International Journal of Scientific & Engineering Research, Volume 8, Issue 4, April-2017
ISSN 2229-5518

Recent Efforts to Improve Microstructure And Weld Properties of Spot Weldments - A Review

Sushil T Ambadkar, Dr. DeepakV.Bhope

ABSTRACT- The type of the joints covered are i) Spot welding of triple-thin-sheet aluminium alloy ii)Resistance spot welding of dual phase steel with external magnetic field iii) Resistance spot welding of three different dissimilar aluminium alloy stackups that included die cast Aural2T7 to Aural2T7,Aural2T7 to AA5754O, and Aural2T7 to AA6022T4 iv)Resistance spot welding behaviour of 780 MPa dual-phase steel with HDGA coating compared to the one coated with HDGI coating.v) Use of post weld heat treatmentusingSecond Pulse Current in Resistance Spot Welding of TRIP Steel and its effects on the Microstructure and mechanical behaviour. The materials considered are Aluminium, DP980, Mild steel and 302 austenitic stainless steel, AISI 430/DQSK Steels and TRIP steel. The changes obtained in microstructure and properties for different welding processes are discussed. In spot welding of triple-thin-sheet aluminium alloy, an analytical model, which is suitable for the three-sheet aluminium alloy resistance spot weld, was proposed to ensure the pullout failure mode. The critical weld button size required to ensure the pullout failure mode was obtained.Medium level of the second pulse current for post weld heat treatmentimproved mechanical properties with desirable pull-out failure modeand fusion zone microstructure consisted of a recrystallized structure of martensite. The microstructure and mechanical performance of dissimilar resistance spot welds between AISI 430 ferritic stainless steel and drawing quality special killed (DQSK) low-carbon steel was discussed with reference to peak load, failure energy, and failure mode during the tensile-shear test.

1.INTRODUCTION

In joining of thin metal sheets, such as in electronic and medical devices, spot welding is the most widely used, in which a small weld is formed between two metal work pieces through localized melting due to resistance heating caused by a passage of electric current. Because of the simplicity of the process, it is easily automated, and once the welding parameters are set, repeatable welds are possible. Resistance spot welding is the main joining method used in automotive industry. The quality of a resistance spot weld is characterized by its nugget diameter, which primarily determines the mechanical performance of the weld .

2.JOINTS UNDER CONSIDERATION

Y. Li, Y. Zhang, Z. Luo, H. Shan, Y. Q. Feng, And Z. X. Ling(Ref. 1) in their study used, 6061-T6 aluminum alloy sheets with thicknesses of 1, 1.5, and 2.0 mm. Two thickness combinations were used in the experiments. From the upper electrode tip to the lower one, the two thickness combinations were 1.0/1.0/1.0 mm and 1.5/1.0/2.0 mm, respectively. Four types of three-sheet joints for each thickness combination were designed, as shown in Fig.1. The sample dimensions used in this study were 100 × 25 mm with a 25-mm-wide overlap area.

Y. B. Li, Y. T. Li, Q. Shen, And Z. Q. Lin(Ref. 2) used dual phase steelwith 0.80 mm thickness and welded with electrode force of 2.6 kN.Tip diameter of the electrode used was 5 mm. The welding current range was 3.8 to 7.9 kA.They developed the magnetic field and evaluated its effect on the properties of the weld.

M. Pouranvari, S. P. H. Marashi, And M. Alizadeh-Sh(Ref. 3) used AISI 430 ferritic stainless steels and DQSK AISI 1004 low-carbon steel as base metals. The thickness of lap welded sheets was 1.5 mm and length 140 mm .Resistance spot welding was performed using a PLC-controlled, 120-kVA, AC pedestal-type RSW machine. Welding was conducted using a 450 truncated cone RWMA Class 2 electrode with an 8-mm face diameter. The welding process was performed with a constant electrode tip force of 3.3 kN.

A. Aravinthan And C. Nachimani(Ref. 4)used mild steel and 302 austenitic stainless steel as base metals. A standard size (200 × 25 × 1mm) for the base metals was prepared and welded according to the weld schedule as lap joints.The experiment used a constant 3 kN of force for the entire weld schedules at increments of 6, 7, and 8 kA. The weld time was varied from 10 to 20

- *Sushil T Ambadkar,AsstProfessor,Department of Mechanical Engineering,Government College of Engineering,Chandrapur*
- *Dr.DeepakV.Bhope,Professor, Department of Mechanical Engineering,Rajiv Gandhi College of Engineering,Research and Technology,Chandrapur*

cycles with 5 as the interval. The electrode tips were 0.5 mm² in the round area.

V. H. Baltazar Hernandez, Y. Okita, And Y. Zhou(Ref. 5) used TRIP steel in the form of 1.0-mm-thick sheet. Resistance spot welds were conducted in a CenterLine Ltd. 250-kVA, singlephase AC resistance spot welding machine. It is a pedestal-type, pneumatically operated machine, with a Robotron™ constant current control and applied a frequency of 60 Hz. As per the ResistanceWelding Manufacturing Alliance (RWMA) standards, truncated Class 2 copper electrodes having a face diameter of 6.0 mm were used. A constant water flow rate of 4 L/min was maintained for cooling the electrodes

3.MATERIALS

The nominal chemical compositions of the materials considered in this review are given in table 1.

TABLE 1

S N	Base Metal	Composition Wt %	Weld details	Ref
1	6061T6 Aluminum Alloy	Si-0.56 Mg-1.10 Zn-0.25 Cu-0.25 Mn-0.15 Fe-0.70 Cr-0.18 Ti-0.15 Al- Balance	Two stack-ups, 1.0/1.0/1.0 mm and 1.5/1.0/2.0 mm, triple-thin-sheet	1
2	Dual Phase steel 980	C-0.150 Si-0.5 Mn-1.5 P-0.010 S-0.002 Al-0.04	Lap joint	2
3	a)AISI430 FSS, b)DQSK Low-Carbon Steel	a)AISI430 C -0.024,Mn-0.513,Cr -17.002,Si-0.383,Ni-0.066,Mo-0.026 DQSK- C -0.044 Cr-0.010,Ni-0.031,Mn-0.202,Si-0.001,S-0.03,Mo- 0.003	Lap joint of AISI 430 FSS to DQSK low-carbon steel	3
4	Mild steel(MS) and 302 Austenitic Stainless Steel (ASS)	MS- C -0.23,Mn-0.90,P -0.04,S- 0.05 302 ASS-C -0.15 Cr- 17–19,Ni- 8–10,Mn-2.00,Si-1.0,S-0.03,P- 0.04	Lap joint	4
5	TRIP Steel	C-0.18,Mn-1.63,P-0.01,Si-1.61,Cu-0.02,Ni-0.016,Cr-0.02,Mo-0.01,Al-0.03	Lap joint	5

4.SPOT WELDING OF TRIPLE-THIN-SHEET ALUMINIUM ALLOY

Y. Li, Y. Zhang, Z. Luo, H. Shan, Y. Q. Feng, And Z. X. Ling [1] investigated failure mechanism of three-sheet 6061-T6 aluminum alloy resistance spot welds, especially the failure mode transition behavior of the spot welds. Four types of joints were designed and the mechanical properties of three-sheet RSWs are also investigated. The joint specification of test specimen is shown in fig 1.

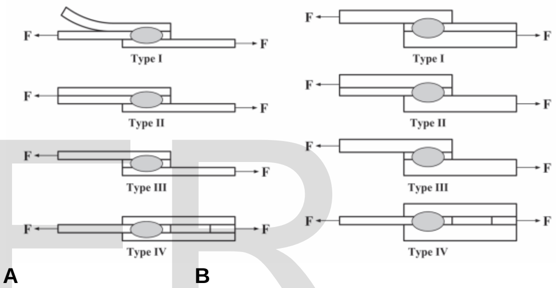

Fig. 1 — Joint designs of the three sheet AA6061T6 welds: A — 1.0/1.0/1.0 mm stack; B — 1.5/1.0/2.0 mm stack.

In the Type I and II joints, only one interface bore the tensile force during the test. In the Type III and IV joints, both of the two interfaces bore the tensile force during the test. Spot welding was performed using a 220-kW direct current (DC) inverter RSW machine. The tensile-shear tests were performed at a crosshead of 1 mm /minwith a CSS-44100 materialtest system. The maximum load of the CSS-44100 material test system is 200 kN and the initial distance between the crosshead was 125 mm (the gripped zone on each sheet was 25 mm). The peak load was evaluated using the average value of the three complete tensile-shear tests. The “button size” was used to evaluate the weld quality rather than the “nugget size” (Ref. 6). Step-by-step tensile-shear tests were used to investigate the failure processes of the weld joints. Seven specimens were obtained from different stages (load raising stage, peak load stage, load drop stage, and final fracture stage) during the tensile-shear test. The seven specimens were ground, polished, and etched using standard metallographic procedures. The cross sections of the welds were etched by Keller's reagent The Vickers micro-hardness test was performed using an indenter load of 100 g for a period of 10 s.

4.1 Microstructure

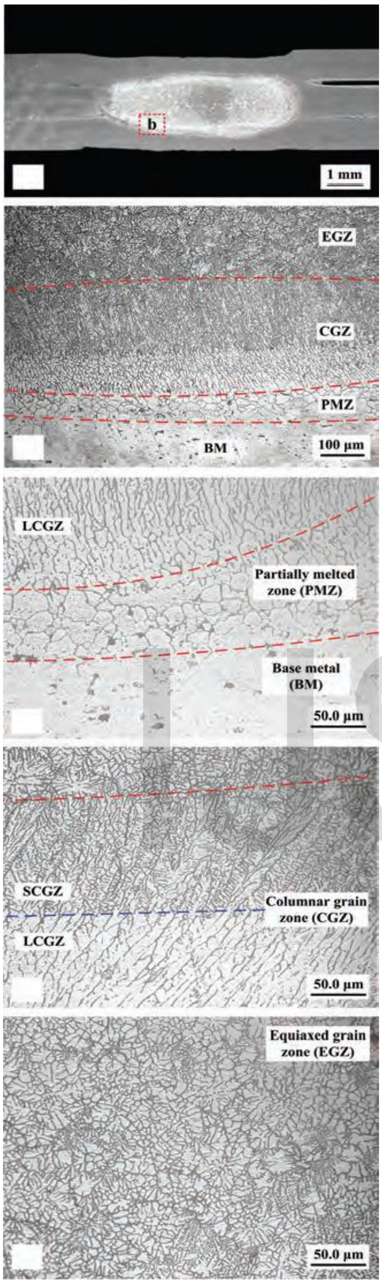

Fig. 2 —Microstructure of the 6061T6 resistance spot weld nugget in the 1.0/1.0/1.0 mm stack

Figure 2 shows the exemplary microstructure of the 6061-T6 resistance spot weld nugget in the 1.0/1.0/1.0 mm stack which was similar to 1.5/1.0/2.0 mm stack. As shown in Fig. 2, fromnugget edge to nugget center, the microstructure is partially melted zone (PMZ), columnar grain zone (CGZ), and equiaxed grain zone (EGZ). The columnar grain has two morphologies, the columnar grain with large secondary dendrite arm spacing (LCGZ) and the columnar grain with small secondary dendrite arm spacing (SCGZ).The authors found that the LCGZ was easier to form at the lower interface (close to the negative electrode) because of the Peltier effect (Refs. 07,08).The lowest micro-hardness appears in the LCGZ, which has a coarser structure and less alloy content.

4.3 Failure Mode Transition in Types I and II (Equal Thickness Stacks)

Three types of failure modes, interfacial (IF) failure, partial thickness, partial pullout (PT-PP) failure (Ref. 09), and pullout (PO) failure were observed in joint Types I and II, as shown in Fig. 3.

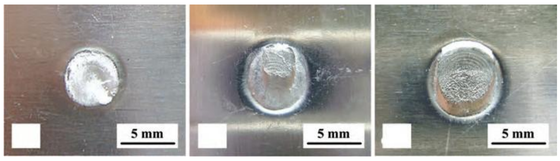

Fig.3— Photos of the failure surface in the 1.0/1.0/1.0 mm stack: Interfacial failure; partial thickness-partial pullout failure; pull-out failure.

The load-displacement curves indicated similarity of the mechanical behavior of the Type I and II joints, as shown in Fig. 4.

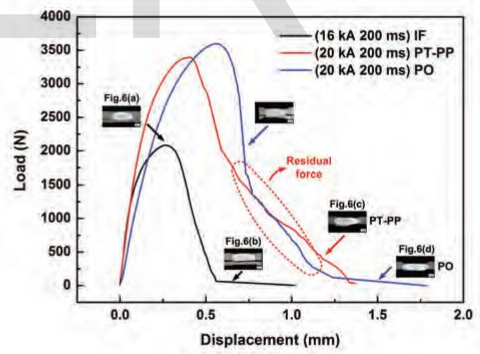

Fig. 4 — Typical load-displacement curves of the Type I and II joint in the 1.0/1.0/1.0 mm stack.

Figures 5a and 5b show the macro/microstructures of the fracture surface cross section of welds that failed in the IF mode. Figure 5a locates the section where the force achieved its maximum value, and a crack formed, explaining the subsequent load reduction. The crack initially formed between the PMZ and LCGZ and then propagated through the interior of the LCGZ, and finally failed as an interfacial characterization — Fig. 5b.

The sub optimized welding parameters (16 kA, inadequate heat input) contributed to the formation of the LCGZ, which has a low hardness and strength to resist the crack propagation. Figures 5c and 5d show fracture initiation location of the welds that failed in the PT-PP and PO mode, respectively.

a **b**

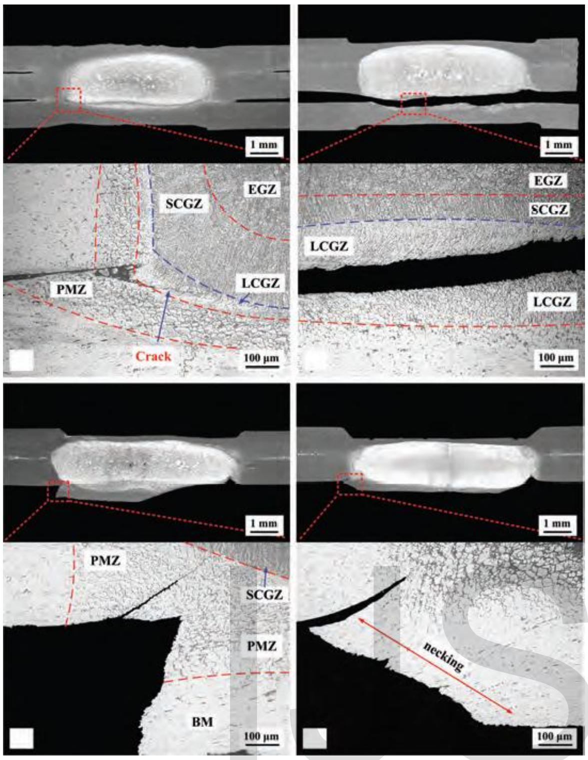

c d

Fig. 5 — Macro/microstructures of Type II weld joints in the 1.0/1.0/1.0 mm stack that failed in a,b — IF mode (16 kA, 200 ms);c — PTPP mode (20 kA, 200 ms); d — PO mode (20 kA, 200 ms).

Figure 6 shows the effect of button size on the peak load and energy absorption of joint designs I and II. Simple linear regression was applied to both the data obtained from joints I and II, and a best fit line with a coefficient of determination (R2) of 0.878, was obtained. The relatively high value of R2 suggested that a linear relationship exists between the peak load and button size. This phenomenon is also observed by Han et al. (Ref. 10) and Sun et al. (Ref. 11).

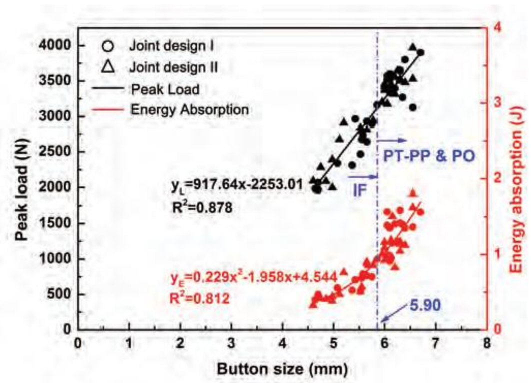

Fig. 6 — Effect of button size on the peak load and energy of joint designs I and II in the 1.0/1.0/1.0 mm stack.

4.4 FAILURE OF JOINT TYPE III AND IV

IF,PT-PP, and PO failures observed in the Type III joint were similar to joint Types I and II and analysis of the PO failure mode was discussed as it was found to be different from the previous case. From Fig. 7, it is clear that the crack began to form at LCGZ and propagated through the SCGZ and LCGZ interface. A crack was also found on the other workpiece/workpiece interface —Fig. 7 indicating competition between the two interfaces in a threesheet spot weld joint, and that failure will occur on the weaker one. It was verified that the LCGZ is the weak area in a spot weld. The PO mode, also indicated competition between the two interfaces for crack during the tensile-shear test.

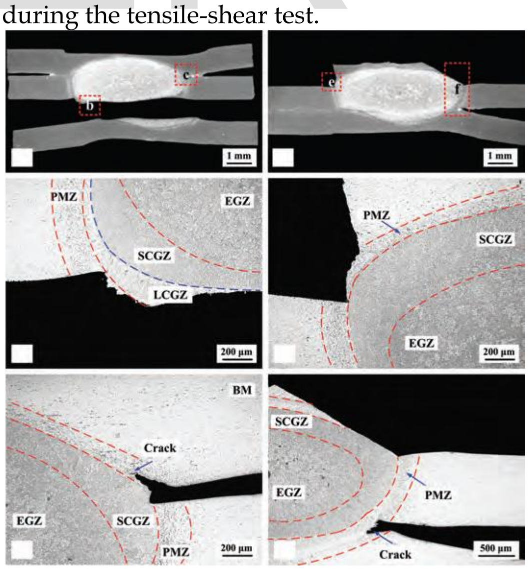

A **B**

Fig. 7 — Macro/microstructures of Type III weld joints in the 1.0/1.0/1.0 mm stack that failed in A, — IF mode; B— PO mode.

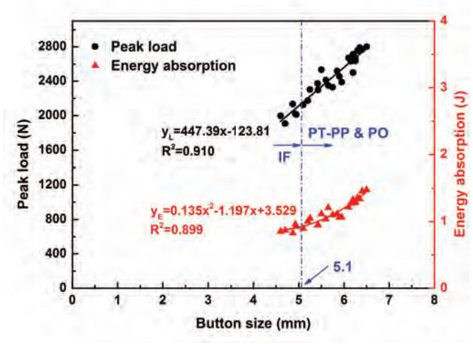

Fig. 8 — Effect of button size on the peak load and energy absorption of the Type III joint in the 1.0/1.0/1.0 mm stack.

Figure 8 shows the effect of button size on the peak load and energy absorption of joint design III. The minimum button size that guarantees a PO mode was 5.1 mm. The results are similar to the case of joint Types I and II.

The failure modes of type IV joint were different from those of joint Types I,II, and III due to pure shear. When the nugget size was small, both of the two interfaces failed through double interfacial failure (DIF). When the nugget size grew larger, joint showed one interfacial/ one pullout (IF/PO) failure. When the nugget size was large enough, thebase metal fractured through base metal fracture (BMF) failure.(Fig 9)

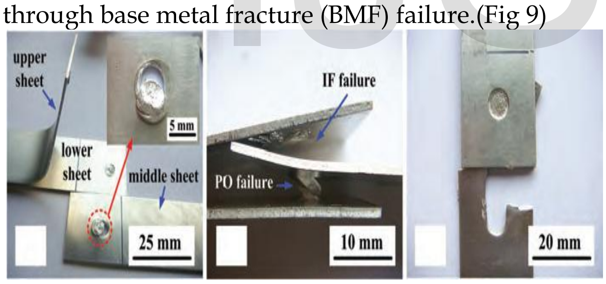

A B C

Fig. 9— Photos of failure modes of the Type IV joint in the 1.0/1.0/1.0 mm stack: A —Double interfacial failure; B — one interfacial/one pullout failure; C — base metal fracture failure.

Figure 10 shows the typical load-displacement curves of the Type IV weld joint that failed interfacially. The load-displacement curve has two peaks. It was seen that the nugget was squeezed and the middle sheet was pulled out along the tensile direction.At the same time, cracks formed and propagated at both of the two interfaces. It can be seen that the micro-hardness of EGZ increased with an increasing deformation degree due to work hardening. Figure 10, shows the fracture occurred in the interior of the LCGZ.

The load-displacement curve of the Type IV weld joint that failed in the IF/PO mode is similar to that in the DIF mode.

Figure 11 shows the load-displacement curve and microstructures of the Type IV weld joint that failed in the BMF mode. The curve has a "platform," which indicates that the crack is propagating in the base metal and, therefore, the load is relatively stable. The weld nugget had very small deformation during the tensile process compared with those that failed in the DIF and IF/PO modes. This indicates that the weld nugget was large enough to resist being squeezed.

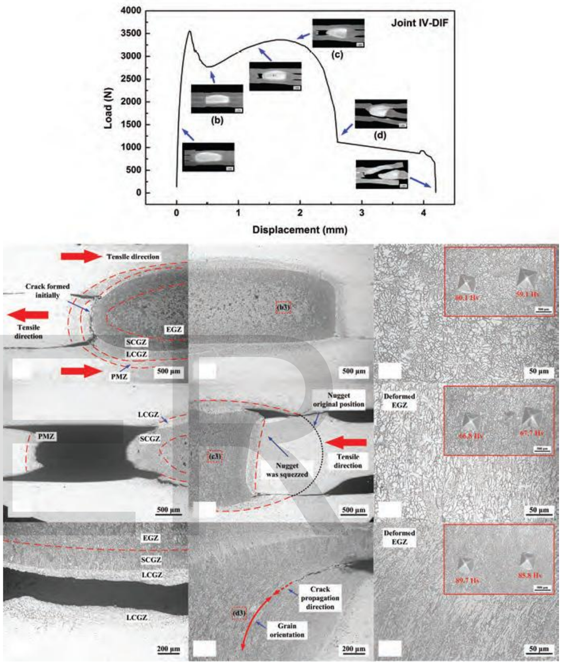

Fig. 10— Typical load-displacement curve and microstructures of Type IV weld joints in 1.0/1.0/1.0 mm stack which failed by the interfacial mechanism (18 kA, 200 ms).

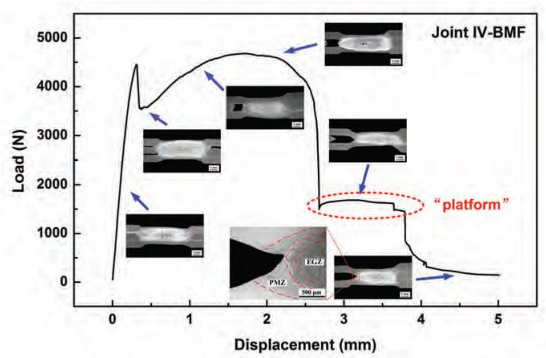

Fig. 11 — Typical load-displacement curve of Type IV weld joints in the 1.0/1.0/1.0 mm stack that failed in BMF mode (22 kA, 200 ms).

ISSN 2229-5518

4.5 Failure Mode Transition in Three Unequal Thickness Stacks

The overall failure rules of the 1.5/1.0/2.0 mm stack were similar to that of 1.0/1.0/1.0 mm stack. For all four types of joints, the IF failure location moved from LCGZ to EGZ and no obvious LCGZ formed in the 1.5/1.0/2.0 mm stack. The critical button size was about 6.2 mm, which is nearly the same as that in the 1.0/1.0/1.0 mm stack (6.25 mm). This indicates that for the joint design of pure shear, the critical weld nugget size or button size may be controlled by the thickness of the middle sheet.(Fig 12)

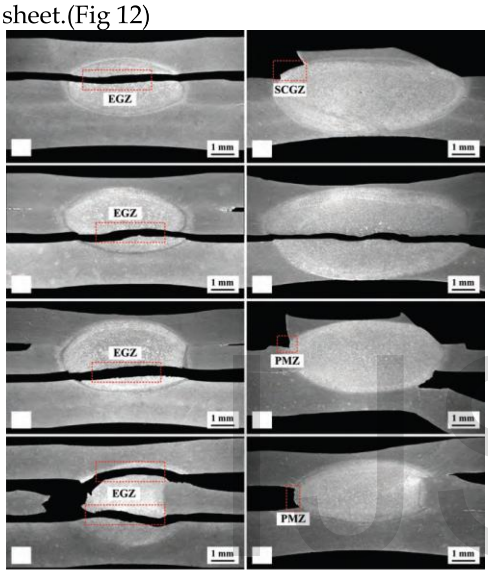

Fig. 12 —Macrostructures of weld joints in 1.5/1.0/2.0 mm stack

4.6 Analytical Model to Predict Failure of Three Sheet Aluminum Spot Welds

Y. Li, Y. Zhang, Z. Luo, H. Shan, Y. Q. Feng, And Z. X. Ling developed an analytical model considering the weld rotation as the weld rotation was not considered by Pouranvari et al. for studying analytical failure model for the RSW ofsteel (Refs. 12, 13).VandenBossche analyzed the stressdistribution when a spot weld failed in the IF and PO modes (Ref. 14). As shown in Fig. 13, once the weld rotates, the load on the weld interface can be decomposed to two components: the force N normal to the faying surface and the force S parallel to it. They are related to F by

$S=F\cos\theta$ and $N=F\sin\theta$

In the tensile-shear test, the driving force for the IF mode is the shear stress at the sheet/sheet interface (Ref. 15). The shear load S generates a shear stress τS distributed across the interface. If the average value of the shear stress is V/A, then the maximumvalue is

$$\tau^{IF}_{SMA}= 3S/2A= 6F\cos\theta_{IF}/\Pi d^2$$ (Ref.14)

where□ IF is the weld rotation angle when the joint experiences IF failure. The driving force for the PO mode is the tensile stress around the nugget (Ref. 15). As shown in Fig. 13, the tensile stress due to S is

$$\sigma_S^{PO}= S / A= S / \Pi dt / 2= 2F\cos\theta_{PO}/\Pi dt$$

where□ PO is the weld rotation angle when joint experiences PO failure. The rotation models of the four types of joints are schematically shown in Fig. 14. It is obvious that the above equations can be applied to the joint Types I, II and III directly.The above model is not suitable for joint Type IV as it experienced pure shear. Letting the maximum shear stress equal to the shear strength of the weld nugget, and then the failure load at the IF mode FIF can be expressed as

$$F_{IF}=\Pi d^2\tau_{WN}/6\cos\theta_{IF}$$

whered is the weld nugget, and□ WN is the shear strength of the weld nugget. For a three-sheet RSW, d was replaced by dIN, which is the weld nugget diameter at the failure interface. Considering that the aluminum spot welds are more sensitive to porosity or voids, porosity factor P was introduced into Equation (Ref. 11)

$$F_{IF}=P\,\Pi d^2_{IN}\,\tau_{WN}/6\cos\theta_{IF}$$

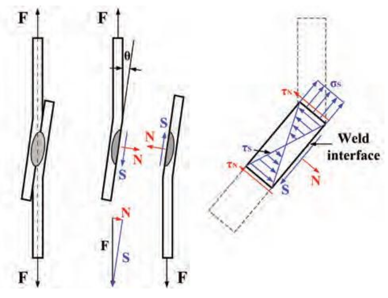

A B C

Fig. 13 — Stress analysis in the weld area: A — Weld rotation; B— IF failure; C — PO failure (Ref. 14).

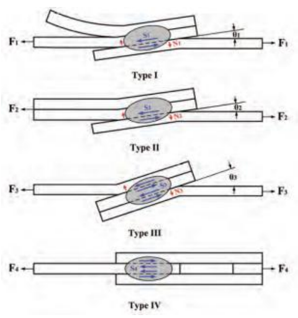

Fig. 14 — Schematic of joint rotation in the 1.0/1.0/1.0 mm stack: Type I joint; Type II joint; Type III joint; Type IV joint in sequence.

Letting the shear stress equal the tensile strength of the pullout failure location, then the peak load for a weld to fail in the pullout mode under the tensile-shear test can be approximated as

$F_{PO}=\Pi d_{IN} t_{ID} \sigma_{FL}/2\cos\theta_{IF}$

In order to ensure pullout failure for a spot weld, FPO <FIF. Thus, the critical nugget diameter DC can be obtained from above two Equations.

$D_C=3t_{ID}\ \sigma_{FL}\cos\theta_{IF}\ /P\tau_{WN}\cos\theta_{PO}$

Applying the linear relationship between the strength and hardness, and the linear approximate between shear strength and tensile strength, Equation was rewritten as

$D_C= 3t_{ID}\ H_{FL}\cos\theta_{IF}/Pf\ H_{WN}\ \cos\theta_{PO}$

whereHFL is the hardness of the failure location, HWN is the hardness of the weld nugget, and f is a constant coefficient. For aluminum alloys, f is about 0.6 (Ref. 16). HWNwas replaced by HLCGZ Therefore, Equation was rewritten as

$D_C= 3t_{ID}\ H_{PO}\cos\theta_{IF}/Pf\ H_{IF}\ \cos\theta_{PO}$

whereHPOis the hardness of pullout failure location, and HIFis the hardness of interfacial failure location.

Above Equation was applied to the Types I and II joints of the 1.0/1.0/1.0 mm stack, the critical nugget diameter for Types I and II joints was 6.0 mm which was very close to the experimental result of 5.9 mm.

In the case of a Type III joint, critical nugget diameter was 5.3 mm, little larger than the experimental value (5.1 mm).

Above equations were not suitable for the Type IV joint because the failure mode of the Type IV joint was different from the other types of joints. This paper constructed a model for predicting the failure mode for the Type IV joint and critical nugget diameter was found to be 6 mm which was smaller than the experimental result (about 6.25 mm).

For the Type I joint of the 1.5/1.0/2.0 mm stack, the failure location in the PO mode was the SCGZ. The critical nugget diameter for the Type I joint was 9.2 mm which was very close to experimental result of 9.1 mm.

For the Type II joint of the 1.5/1.0/2.0 mm stack, all the joints failed in IF mode, assuming that the PO failure location of Type II joint is the PMZ and the rotation angle is the same as Type I joint. The critical nugget diameter for Type II was 11.3 mm. However, the maximum button size obtained from experiments was about 10 mm.

For the Type III joint of the 1.5/1.0/2.0 mm stack, the IF failure location was the LCGZ, while the PO failure location was the PMZ. Thus, the critical nugget diameter for the Type III joint was found to be 8.4mm.The predicted value was very close to the experimental result of 8.2 mm.

For the Type IV joint of the 1.5/1.0/2.0 mm stack, it can be seen that in the DIF failure (Fig. 12), both of the two interfaces failed through the EGZ. Accordingly, the critical nugget diameter was 6 m, close to the predicted result of the 1.0/1.0/1.0 mmstack.

5.SPOT WELDING OF DUAL PHASE STEEL WITH EXTERNAL MAGNETIC ASSISTANCE

Y. B. LI, Y. T. LI, Q. SHEN, and Z. Q. LIN(Ref 2) have studied spot welding of dual phase steel with magnetic assistance. They proposed a finite element (FE) model to investigate the effect of two different modes of EMF on the Magnetically Assisted –Resistance Spot Welding process (MA-RSW). The material composition is given in table 1.

Figure 15A shows the RSW system used by Y.B.Li and others. It includes a Fanuc robot with specification R2000-Ib210f withsix degrees of freedom, Fanuc AC servo motor α8/4000is, Medar 5000s medium frequency direct current welding controller,and Obara C-type welding gun equipped with two dome-shaped electrodes..Specifically, the electrode cap with composition Cr- 0.7%, Zr-0.1%, Cu>98.5%. was used. Tip diameter of the electrode cap was 5.0 mm.

On EMF studies, two modes of EMFs generated by a single and a pair of permanent magnets werediscussed. But only the EMF under a pair of permanent magnets was validated using FE model. Figure 15B shows the setup of the two magnets.

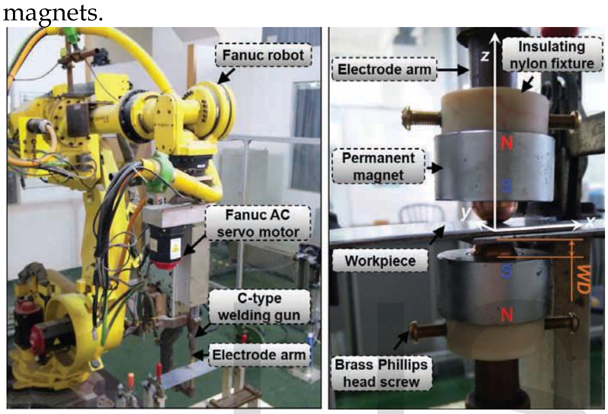

Fig. 15 — MA-RSW equipment. A — RSW system; B — EMF source, N: N pole of the magnet, S: S poleof the magnet; WD: working distance of the permanent magnet

Y.B.Li and others used two magnets locatedsymmetrically with their south poles (S) against each other. A coordinate origin was set at the intersection point ofthe electrode central axis and the faying surface of work pieces as shown. Distance from the S pole of a magnet to the tip of the nearestelectrode was defined as working distance (WD). In order to verify the accuracy of the FE model, the calculated and measured values of the EMF distributions on the faying surface of work pieces were compared and found to be in good agreement.

5.1 Analysis of Weldments Welded with Magnetic Assistance

The analysis was done by analysing effect of EMF mode on Nugget Formation, effect of EMF Intensity on Nugget Size, weldability of MA-RSW Process and judging sensitivity of the MA-RSW Processto Welding Current.

5.1.1 Effect of EMF mode on Nugget diameter and thikness.

In many cases, the nugget diameter is used as the sole parameter to describethe quality of a spot weld. Results showed that increasing the nugget diameterwill enhance weld strength (16–18) and raise the probability of button pulloutfracture (18, 19).Nugget formation of the MA weldsunder different EMFs was presented incurves in Fig. 7.

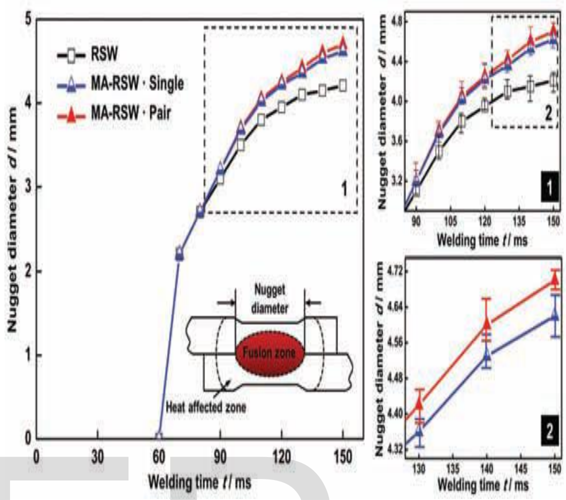

Fig. 16 — Nugget diameter growth process along with the welding time (welding current, 6.0 kA; welding time, 150 ms; WD, 3 mm).

It can be seen that at the early stage ofnugget formation, the nugget size of the three types of welds was almost the same. Starting from approximately 90 ms, thenugget diameters of these two types ofMA welds were both wider than that of thetraditional weld, and such difference graduallybecame more obvious with the heataccumulation in the middle-late weldingstage. Moreover, the diameter growth rateof the MA weld under a pair of permanentmagnets was faster than that under a singleone, especially in the late weldingstage.During the middle-latewelding stage, more molten metal wouldbe brought to the edge of the growingnugget driven by the external magneticforce so as to further promote the nuggetdiameter growth. Moreover, for these twotypes of MA welds, since the external magneticforce generated by a pair of magnetswas stronger, the diameter growth rate ofthe weld was correspondingly faster.Figure 17 shows the metallographicviews of the nuggets after 150 ms of weldingtime. Affected by the EMF, the nuggetdiameter obtained under a single and apair of permanent magnets was not only increasedby 9.7 and 11.6%, the ellipsoidal nuggetobtained in traditional weld, was replaced by pea nutshell-shapewith the edge thicker thanthe middle, as shown in Fig. 17B and C.

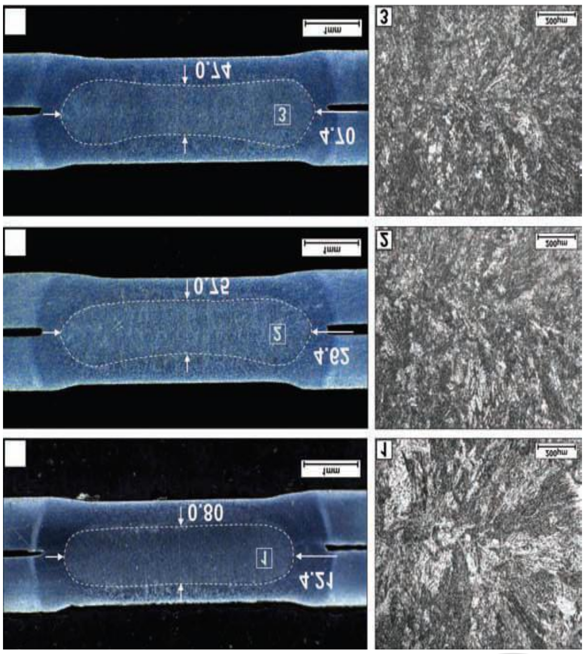

Fig. 17— Typical cross-sectioned weld nugget and the microstructures in the weld nugget.A — Traditional weld; B — MA weld under a single permanent magnet; C — MA weld under a pair of permanent magnets (welding current, 6.0 kA; welding time, 150 ms; WD,3 mm).

By comparingFig. 17B and C, itcan be seen that the symmetry of thenugget under a single permanent magnetwas relatively poorer due to shifting of ends of thenugget slightly upward. Suchnugget offset is usually not preferred whenwelding two sheets with equal thickness.The difference in EMF mode not onlychanges the nugget shape, but also affectsthe microstructures within the nugget. Asshown in Fig. 17,under a pair ofpermanent magnets, the oriented growthof the dendrites toward the faying surfacewas less directional, and the boundary ofthe faying surface was also less visible.Therefore, compared with the MAweld under a single magnet, the MA weldunder a pair of magnets has exhibited betterquality in view of nugget symmetry,nugget diameter, and nugget microstructures.

5.1.2 Effect of EMF Intensity on Nugget Size

Intensity of the EMF can be adjustedby changing WD. Variations of the horizontalcomponent of the EMF flux densityalong the x-axis of the 0- to 3.5-mm radiuswelding region under different WDs weredescribed in Fig. 18

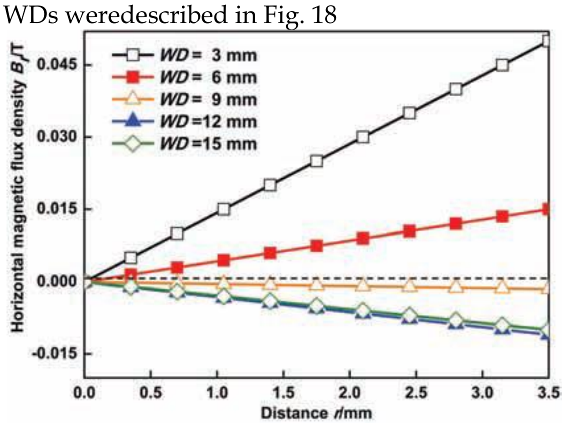

Fig. 18— Intensity of the horizontal component of the EMF under a pair of permanent magnets along the x-axis in the 0- to 3.5-mm radius welding region.

It is clear that,the horizontal componentwas strongest when WD was set to 3 mm,; it was weaker when WD wasset to 6, 12, and 15 mm;intensity of thehorizontal component was close to zero when WD was set to 9 mm.Figure 10 shows the nugget size variationsof the MA weld along with thechanges in WD.

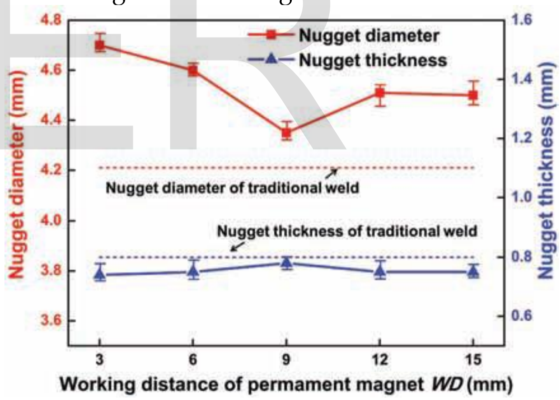

Fig. 19 — Nugget size variations of the MA welds under a pair of permanent magnets along with the changes in WD (welding current, 6.0 kA; welding time, 150 ms).

Broken lines in the graph shows data of a traditional weld under identical welding parameters. It is clear from plot that the nugget ofthe MA weld was the widest and thinnest when the horizontal component of the EMF was strongest under 3-mm WD.By contrast, when the horizontal componentwas the weakest under 9-mm WD, thenugget of the MA weld was the narrowestand thickest. Moreover, compared withthe nugget thickness, the nugget diameterwas more sensitive to the variations ofEMF intensity. Since the nugget diameteris well acknowledged as the major criteriawhen evaluating the quality of a RSWweld, it is acceptable to suggest that thestronger the horizontal component of theEMF within the welding region is, the betterthe weld quality will be.

5.1.3 SENSITIVITY OF THE MA-RSW PROCESS TO WELDING CURRENT

In MA-RSWprocess, the total heat input depends on current density and current density also greatlyaffects the intensity of the electromagneticforce. Sensitivity of the MA-RSWprocess to the welding current was discussed by tensile-shear testing on the traditionalwelds and MA welds under differentwelding currents. An extremely strong weld is said to be obtained if a button-pullout fracture develops only within the base metal, and a hole is left in each of the steelsheets. A comparatively less strong weld is indicated by abutton-pullout fracture developed within both the base metal and heat-affected zone, and a hole is left in one of the steel sheets.For typical interfacial fracture ,full separation of the faying surface of workpieces occursas a result of fracture through theweld.
Sensitivity of the process could be explained by the differences in fracture modes under different welding currents.Itwas observed that due to increasein nugget diameter shown in Fig. 17,the tensile-shear strength of the MA welds were strongerand elongationat break of the MA welds was higher than that of thetraditional ones. These observations were more prevalent for welds under relatively low welding current than that of for welds under relativelyhigh welding current.The increase in nugget diameterand refinement of solidified microstructuresin MA welds would lead to the relativelyobvious improvement of weld strengthand ductility at low currents.With the help of load versus displacementcurves of welds under different weldingcurrents ,it wasinferred that affected by the EMF, theprobability of weld button-pullout fracturefor DP980 steel was raised, which indicatedthe enhancement of energy absorptioncapacity under impact loading,especially under low welding current.

5.1.4 WELDABILITY OF MA-RSW PROCESS

Weld lobe diagram was used to make comparison between the traditionalRSW and MA-RSWprocess. Results areshown in Fig. 20.

The left boundaryof weld lobe diagram shows minimum nugget diameter, about 3.6 mm . The rightboundary of weld lobe diagram shows the threshold valueof welding current; beyond which expulsionwill occur.It can be seen that affected bythe EMF, the right boundary of theweld lobe diagram of the MA-RSWprocess moved leftward by nearly400 A.In case of high welding current and welding time, a lot of high-temperature moltenmetal would rush to theedge of the growing nugget due to the strong fluid flow driven by the circumferential magneticforcewhichcould induce expulsion during the MA-RSW process. From the practical pointthis is a negativeaspect of the MA-RSWprocess. On the other hand, due to theincrease in nugget diameter, theleft boundary of the weld lobe diagramof the MA-RSW process alsomoved leftward by approximately400 A. The overall width of the weldlobe diagram remained almost unchanged .Thus under proper welding parameters,the MA-RSW process could bean alternative way to guaranteeweld quality as well as reduce energyconsumption.

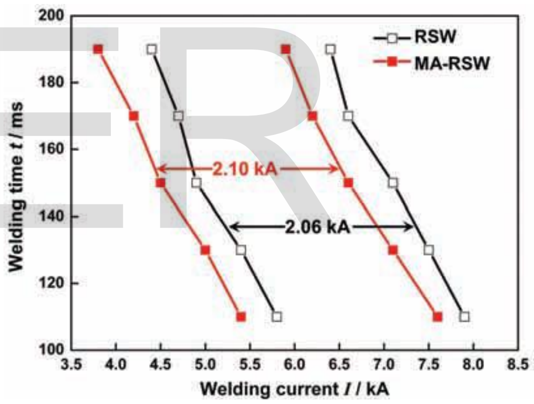

Fig. 20— Comparison of weld lobe diagram between the traditionalRSW and MA-RSW process (WD, 3 mm).

Qi Shen ,YongBing Li , ZhongQin Lin and GuanLong Chen (Ref 16) observed that the EMS-RSW welds showed longer fatigue life underdynamic tensile-shear loads, particularly in high cycle conditions.

6.WELDING OF DISSIMILAR AISI 430/DQSK STEELS RESISTANCE SPOT WELDS

M. Pouranvari, S. P. H. Marashi, And M. Alizadeh-Shinvestigated the welding metallurgy of dissimilar RSW of ferritic stainless steel and DQSK low-carbon steel as base metals sheets with.thickness of 1.5 mm. Resistance spot welding was performed using a PLC-controlled, 120- kVA, AC pedestal-type RSW machine.

Welding was conducted using a 45- deg truncated cone RWMA Class 2 electrode with an 8-mm face diameter. The welding process was performed with a constant electrode tip force of 3.3 kN. The welding current was increased from 6 to 11 kA with an increment of 0.5 kA. Throughout the process, squeeze, welding, and holding times were kept constant at 40, 12, and 20 cycles, respectively. To evaluate the mechanical performance and failure mode of the spot welds, the tensile-shear test was performed. The tensile-shear test samples were prepared according to ANSI/AWS/SAE/D8.9-97 standard (Ref. 17).Figure 24A shows the tensile-shear sample dimensions. Failure modes were determined from the failed samples. Peak load (measured as the peak point in the load-displacement curve) and failure energy (measured as the area under the load displacement curve up to the peak load) were extracted from the load displacement curve — Fig. 24B. The amount of failure energy was calculated by measuring the area under the load-displacement curve up to the peak load. Microstructure characterization of the weldment was conducted by performing standard metallography procedure.The FZ size was measured on the metallographic cross sections at the low-carbon steel side. A Vickers microhardness test was performed to obtain a diagonal hardness profile using an indenter load of 10 g.

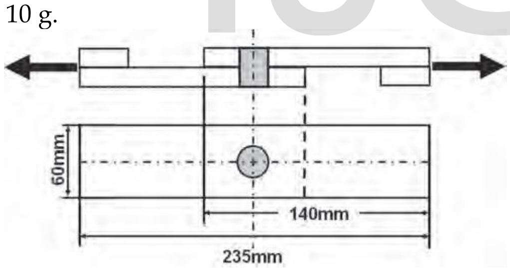

A

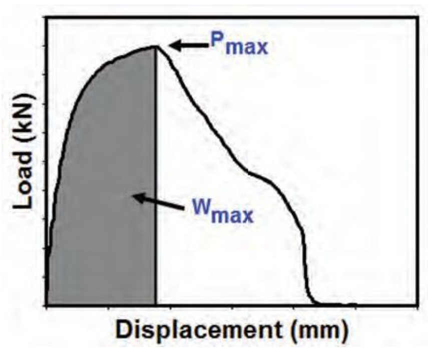

B

Fig. 24— A — The tensile-shear specimen dimensions; B — a typical load-displacement curve along with the extracted parameters. P_{max}: Peak load, W_{max}: Energy absorption.

6.1 Metallurgical Characteristics of HAZ of AISI 430 Steel

Figure 25A shows the microstructure of the AISI 430 base metal indicating a fully ferritic microstructure along with evenly distributed carbides. In the HAZ, microstructure is influenced by phase transformations induced by the welding thermal cycle. Figure 25C shows the microstructure gradient in the HAZ of the FSS side. The phase transformations in the HAZ of AISI 430 steel welds have been discussed elsewhere (Ref. 18). According to the temperature distribution, the HAZ was divided into two distinct metallurgical transformation zones, namely high-temperature HAZ (HTHAZ) and low-temperature HAZ (LTHAZ). The phase transformations in these zones are detailed as follows:

6.1.1 HTHAZ - Based on the pseudo-binary diagram (Fig. 25B), in this region, BM microstructure transforms to fully □ -ferrite microstructure at the elevated temperature. The carbide precipitates in the BM are completely dissolved. Upon cooling, a ferritic microstructure is retained and some reprecipitation of the carbides occurred — Fig. 25D. The absence of a high-temperature austenite phase in the HTHAZ has two consequences: The austenite at the grain boundaries at elevated temperature can act to inhibit ferrite grain growth by pinning the grain boundaries. Therefore, ferrite grain growth at this region can be quite dramatic, as is evident from Fig. 25C. As can be seen, the graingrowth is inversely proportional to the distance from the fusion line. Any austenite that may have formed at the elevated temperature will transform to martensite during the cooling cycle. Therefore, due to the absence of the high-temperature austenite, an almost martensite-free microstructure is formed in HTHAZ during cooling — Fig. 25C.

6.1.2 LTHAZ. Based on the pseudo-binary diagram (Fig. 25B), in this region, the BM microstructure transforms to □ -ferrite plus austenite at the elevated temperature. The amount of austenite at the grain boundaries of □ -ferrite strongly depends on the carbon content of the alloys. Due to the low carbon content of the investigated AISI 430 steel (i.e., 0.024 wt-%), a very limited amount of austenite is formed in the LTHAZ. The high-temperature austenite is transformed to martensiteduring cooling. According to Fig. 25E, there is a small amount of martensite at the grain boundaries in the LTHAZ. Moreover, some reprecipitation of the carbides occurred.

A B

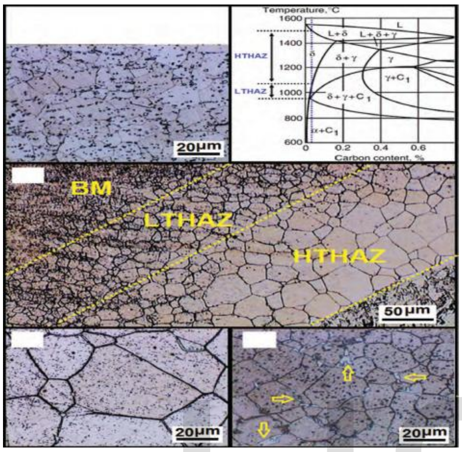

D E

Fig. 25 — A — Base metal microstructure of AISI 430 steel; B — Fe-17% Cr-C phase diagram and HAZ of AISI 430 steel; C — microstructure gradient in the HAZ of ferritic stainless steel; D — grain growth and dispersion of carbide precipitates in HTHAZ; E — martensite formation, indicated by arrows, in LTHAZ.

6.2 HAZ OF DQSK STEEL

Figure 26 shows HAZ microstructure of the DQSK steel side is more heterogeneous than that of the FSS side due to martensitic and eutectoid transformations. According to the temperature distribution, the HAZ of the DQSK steel side can be divided into two distinct metallurgical transformation zones, including upper-critical HAZ and inter-critical HAZ. The phase transformations in these zones are detailed as follows:

6.2.1 UPPER-CRITICAL HAZ (UCHAZ).

This region experiencing peak temperatures above Ac3,can be divided into the following zones: coarse-grained HAZ (CGHAZ)and fine-grained HAZ (FGHAZ).In CGHAZ, which is adjacent to the FZ, both the high cooling rate and large austenite grain size coupled with the formation of the carbon-rich austenite promote the formation of the martensite (Ref. 19). As can be seen, the microstructure CGHAZ consists of martensite, grain boundary ferrite, and Widmanstätten ferrite — Fig. 26. Martensite formation in the FZ is attributed to the high cooling rate of the RSW process due to the presence of water-cooled copper electrodes and their quenching effect as well as short welding cycle.

6.2.2 Inter-Critical HAZ (ICHAZ). In this region, the peak temperature is between Ac1 and Ac3, and the BM microstructure transforms into ferrite plus austenite during heating and austenite can transform subsequently into the martensite, bainite, or ferrite/pearlite depending on the cooling rate and hardenability of the steels. In the case of DQSK steel, the microstructure consists of fine ferrite grains and pearlite, which pearlite amount decreases as it gets closer to BM — Fig. 26. The volume fraction of pearlite in the ICHAZ is higher than that of in the BM due to reaustenization in the ICHAZ. Decreasing peak temperature in the intercritical region (i.e., by moving away the FZ line) results in lower pearlite volume fraction. As can be seen in Fig. 26, the ICHAZ is evidenced by fuzzy pearlite.

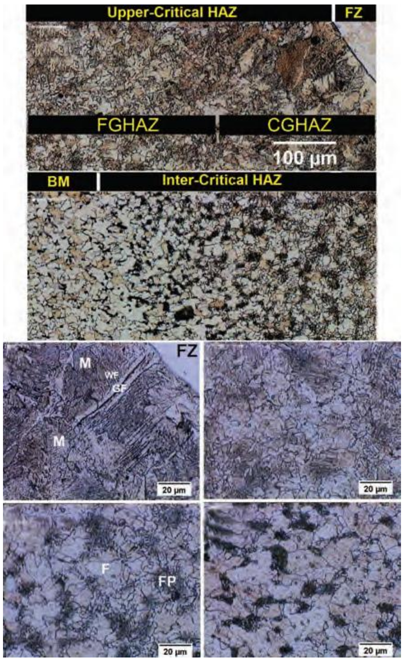

Fig. 26 — Microstructure gradient in the HAZ of low carbon steels. Upper-critical HAZ, including CGHAZ and FGHAZ; inter-critical HAZ; detailed microstructure of CGHAZ; detailed microstructure of ICHAZ. The distance from fusion zone boundary is increased by moving from D to F. (M, F, WF, GF, and FP are martensite, ferrite, Widmanstätten ferrite, grain boundary ferrite, and fuzzy pearlite.)

6.3 Fusion Zone

Figure 27A and B shows the microstructure with volume fraction of ferrite and martensite as calculated 28 and 72%, respectively. For FSS/DQSK welds, the melting ratio is considered as 60/40. Therefore, the FZ chemical composition of FSS/DQSK welds is

Fe-10.2,Cr-0.03C-0.038 Mn- 0.23Si-0.04Ni-0.01.

Considering the low carbon content of the FZ, the Fe-Cr binary phase diagram was used as a reference to track phase transformations in the FZ of the FSS/DQSK weld. Under the non-equilibrium cooling condition, the formed austenite was transformed to martensite. Regarding the transformation of austenite to martensite in the FZ, three points were considered.

6.3.1 Austenite Stability - Self et al.(Ref. 20) in their work on the austenite stability obtained an expression for the martensite start temperature (Ms) as a function of alloy composition. Their equation is given as follows:

M_s= 526 – 12.5 Cr – 17.4 Ni – 29.7 Mn – 31.7 Si – 354 C – 20.8 Mo – 1.34 (CrNi) + 22.41 (Cr +Mo)C

According to Lippold and Kotecki (Ref. 21), equation was accurate to examine austenite stability and estimate martensite start temperature for stainless steels. For FSS/DQSK welds, the Mswas calculated as 3900C indicating that the austenite is not stable at room temperature, and it transformsto martensite, as was observed.

6.3.2 Volume Fraction of Martensite.

According to metallographic examination, 28% ferrite is retained in the microstructure. The volume fraction of martensite in the FZ depends on the volume fraction of austenite present in the weld nugget at high temperatures, which is controlled by □ Ferrite toAustenite phase transformation.. Upon a rapid cooling process (e. g., welding), the transformation □ Ferrite toAustenite has less time to occur. Therefore, the phase transformation sequence in the FZ of dissimilar FSS/DQSK welds under rapid cooling of RSW showed martensite and □ Ferrite.

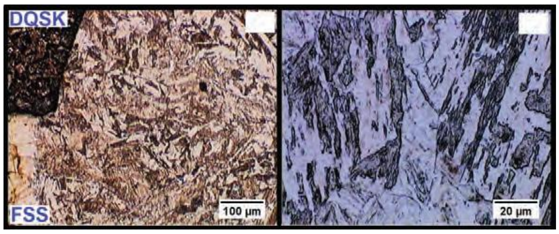

A B

Fig. 27 — A and B — Fusion zone microstructure of FSS/DQSK dissimilar resistance spot weld.

6.3.3 FZ Microstructure Prediction Using Conventional Constitution Diagrams.

It has been proved that the conventional constitution diagrams (e. g., Schaeffler diagram and Balmforth and Lippold) can be used to predict the FZ microstructure of arc welds of joints involving stainless steels (Ref.22). Since the cooling rate in RSW is much higher than the arc

International Journal of Scientific & Engineering Research, Volume 8, Issue 4, April-2017
ISSN 2229-5518

welding, a higher volume fraction retained □ Ferrite is formed in the FZ of the weld made using RSW. Therefore, the presence of a high-volume fraction of □ Ferrite can be attributed to the rapid cooling rate of RSW, which suppresses the completion of post-solidification transformation of ferrite to austenite. Therefore, some corrections should be incorporated to the conventional constitution diagrams to accurately predict the microstructure of the FZ in resistance spot welded joints involving stainless steels.

6.4 Hardness Characteristics.

Figure 28 shows a typical hardness profile of FSS/DQSK welds. Hardness variation across the joint was analyzed in terms of the microstructureevolution in the FZ and HAZs.The hardness of the HAZ in the DQSK is higher than that of the ferritic base metal due to the formation of martensite and pearlite in these regions, respectively. The hardness of the HAZ in FSS was higher than that of the AISI 430 base metal. The higher hardness of the HTHAZ compared to the BM was due to the precipitation of carbides. The higher hardness of the LTHAZ compared to the HTHAZ was due to martensite formation in ferrite grain boundaries and its finer grain size. The hardness of the FZ is higher than both that of the base metals and HAZs, which can be attributed to the martensite formation in the FZ. The peak hardness in the HAZ of the DQSK is lower than the FZ hardness. The ferrite and martensite formed in the FZ are harder than those in the HAZ of DQSK. This can be related to the fact that ferrite and martensite phases in the FZ are enriched in chromium (Cr), an element that can strengthen both ferrite and martensite via a substitutional solid solution strengthening mechanism.

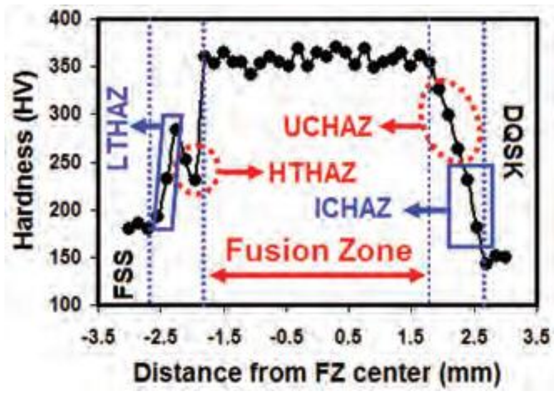

Fig. 28 — Typical hardness profile of dissimilar AISI 430/DQSK resistance spot welds.

6.5 Failure Mode

Both interfacial failure (IF) and double pullout failure (DPF) modes were observed during the tensile-shear testing of the FSS/DQSK welds.The effect of welding current as shown in Fig. 29,not only indicated the enlargement of the weld nugget by increasing welding current, but the failure mode was changed from IF to DPF. To avoid IF mode, a minimum welding current of 7 kA and minimum FZ size of 4.18 mm should be used for welding of the FSS/DQSK joint.

To analyze the failure mode transition of spot welds during the tensile-shear loading, a model proposed byPouranvari and Marashi (Ref. 23) to predict the minimum FZ size (DC) to ensure the pull-out failure mode was used.

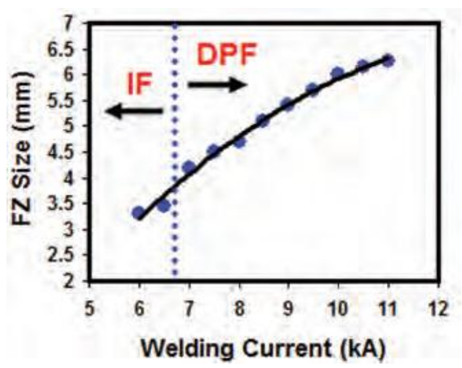

Fig.29 — Effect of welding current on the FZ size and failure mode of dissimilar AISI 430/DQSK resistance spot welds.

As mentioned above, all spot welds made at a welding current higher than 6.5 kA failed at double pullout mode. No single pullout mode was observed. Figure 30A shows the fracture surfaceof welds failed in pullout mode,indicating that the nugget is withdrawn from both sheets (i.e., doublepullout mode). Figure 30B shows the metallographic cross section of a typical weld failed in DPF mode. Figure 30C is a representative load-displacement curve of the FSS/DQSK dissimilar weld. The pullout failure mechanism of spot welds in the tensile-shear loading is dominated by necking of the base metals. In the DPF, the nugget is completely torn off from the sheet, which experiences severe necking.According to Fig. 30B and C, the PF of FSS/DQSK welds can be dividedinto the following stages:

Stage I. Both base metals are work hardened under loading and experienced through thickness straining.

Stage II. The failure is started by severe necking of one sheet. In this case, the PF location is determined by the competition between the necking of DQSK and FSS steel sheets. Since tensile strength and hardness of the DQSK is lower than that of the FSS sheet, DQSK sheet experiences a severe necking leading to the initiation of the failure at this point.

Stage III. After the welds experienced the first crack in the DQSK, the nugget is still connected to the other sheet. The final stage of the fracture occurs by partial separation of the nugget from the FSS sheet.

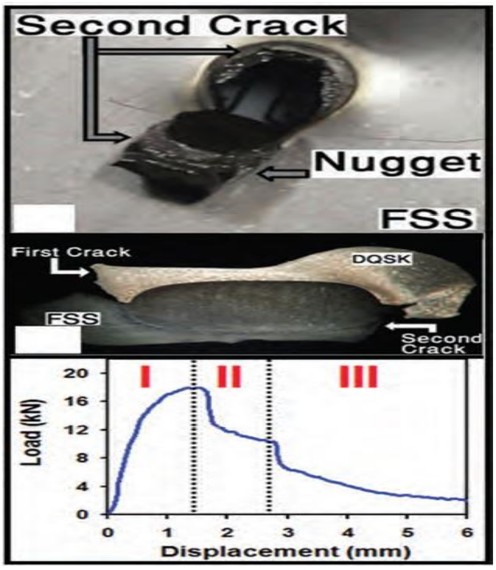

Fig. 30 — A typical DPF mode; macrographic of failure cross section; typical load-displacement curve showing a three-stage failure process.

Stage I: work hardening and through thickness straining of both sheets. Stage II: severe necking and occurring the first crack in the DQSK steel. Stage III: second crack in the FSS side.

6.6 Mechanical Properties

To explore the mechanical properties of the spot welds, peak load and energy absorption were measured. Figure 31A indicated that the welding current has a significant effect on the load carrying capacity and energy absorption capability of the spot welds under the tensile-shear static test. Load carrying capacity and energy absorption capability of spot welds depend on their physical attributes ,especially weld nugget size, failure mode, and failure location strength. According to Fig. 31B, the weld nugget size significantly affects the load-displacement characteristics of dissimilar FSS/DQSK welds. To examine the relationship between the peak load and failure energy and weld nugget size, a scatter plot of peak load (and failure energy) vs. weld size wasconstructed. Since the weld nugget has a asymmetrical shape, the FZ size at sheet/sheet interface in the DQSK steel, which is smaller than that of the FSS side, was measured. Fig. 31C showed a general linear relationship between the peak load (and also failure energy) and FZ size.

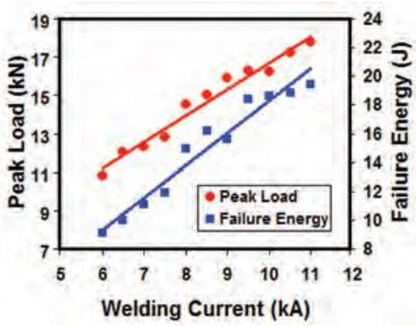

A

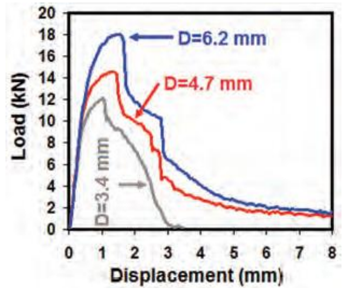

B

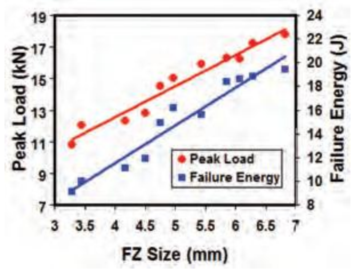

C

Fig. 31 — A — Effect of FZ size D on the load-displacement characteristics during the tensile-shear testing; B — welding current vs. peak load and energy absorption; C — fusion zone size vs. peak load and energy absorption of dissimilar AISI 430/DQSK resistance spot welds.

7.ANALYSIS OF SPOT WELD GROWTH IN MILD AND STAINLESS STEEL JOINTS

A. Aravinthan And C. Nachimani(Ref 4)investigated the effect of the current and weld time on the weld growth, while the electrode tips and force remained constant. They carried entire work to observe the weld growth in mild steels joints, stainless steels joints, and both steels in a mixed joint for the same current and weld time. A total of 200 pairs of welded samples were developed for tensile, hardness, and metallurgical tests

The base metals for these experiments were mild steel and 302 austenitic stainless steel the composition of whom is elaborated in table 1.

Initially, a weld schedule (Table 2) was developed to accomplish the experiments.

Table 2 Test schedule used by A. AravinthanAnd C. Nachimani

Samples number	Material(a)	Electrode tip mm^2	Force kN	Current kA	Weld Time(CYCLE)
1-5	MS AND SS	0.5	3	6	10
6-10	MS AND SS	0.5	3	6	10
11-15	MS AND SS	0.5	3	6	10
16-20	MS AND SS	0.5	3	7	15
21-25	MS AND SS	0.5	3	7	15
26-30	MS AND SS	0.5	3	7	15
31-35	MS AND SS	0.5	3	8	20
36-40	MS AND SS	0.5	3	8	20
41-45	MS AND SS	0.5	3	8	20

(a) MS – Mild Steel; SS – Stainless steel

A standard size (200 × 25 × 1 mm) for the base metals was prepared (Fig. 32) and welded according to the weld schedule as lap joints.

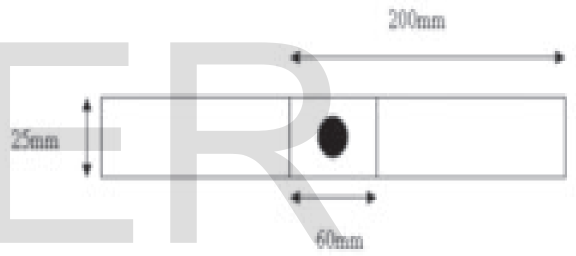

Fig. 32 — Test sample.

7.1 ANALYSIS USING HARDNESS TEST

Figure 33 shows the Rockwell hardness of the mild steel specimen. It was found that the averagehardness of un-weldedareas was 54 HRB, and the averagehardness of welded areas was 98 HRBshowing hardnessincrement of 44 HRB.This increase in hardness can be attributed to heat treatment due tohigh thermal conductivity and low resistivityof the materials (Ref.24).The hardness of the welded areas for the mild steel seemed to be higher than the stainless steel and the mixed steels.

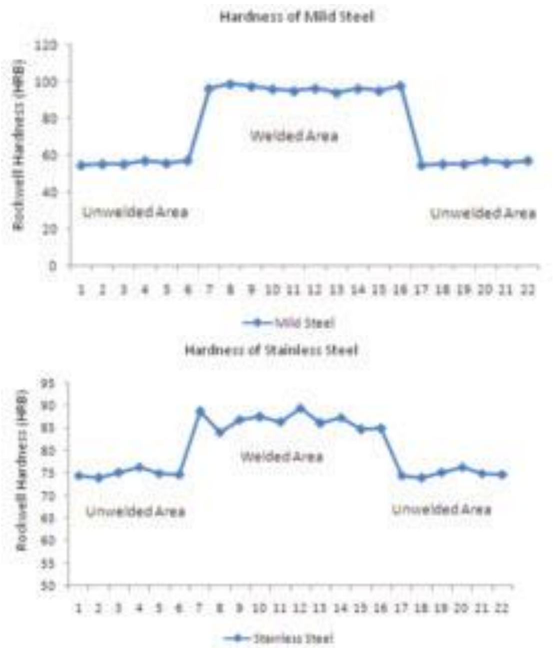

Fig. 33— Hardness diagram for mild steel and Austenitic Stainless Steel

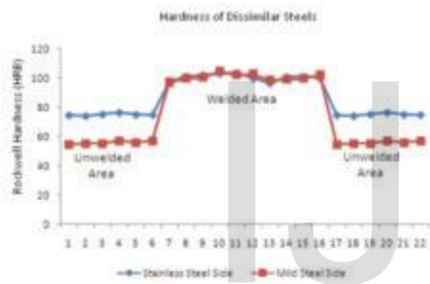

Fig. 34 — Hardness diagram for stainless and mild steels joined.

The variation in hardness of 302 austenitic stainlesssteels was very less as compared to mild steels as shown in fig 33. The average hardness of un-welded area was 75 HRB and the average hardness of welded area was 85 HRB, the increment in hardness being only 10 HRB. The heat treatmenteffect was not supported by thechromium composition of the material(Ref. 25). The effect was reduced by thethermal conducting factors as well as theelectrical resistance.

The final test on hardness was carried out on the dissimilar metalviz mild steel and austenitic stainless steel welded sheets. The hardness increased slightly on both sides of the weld compared to theindividual mild and stainless steels weldmentscategories. The welded region of mild steel showed hardness of 100 HRB,a slight increase of 2 HRB compared to the mild steel category of 98 HRB. The hardness of stainless steel side also increased almost to the mild steelvalues (101 HRB)from 85 to 101 HRB..

The hardness values are plotted against each other in Fig. 34.

7.2 Analysis using Tensile Test

Tensile test results showed increase in strength with increase in welding current and weld time,asreported in the literature (Refs. 25, 26). This was because an increase in current and weld time caused the weld diameter to increase, and therefore the weld strength increased. The amount of heat generated at the weld interface increased as the weld current and weld time increased. It must be noted that the experiments were not conductedbeyond the expulsion limit to seethe extreme cases and were conducted to seethe weld nuggets growth, and therefore,the weld schedule was limited to a fewsteps from poor welds to sound welds. The experimentsthat followed also showed the same principlesof increase and decrease when theparametric changes occurred — Fig. 35.

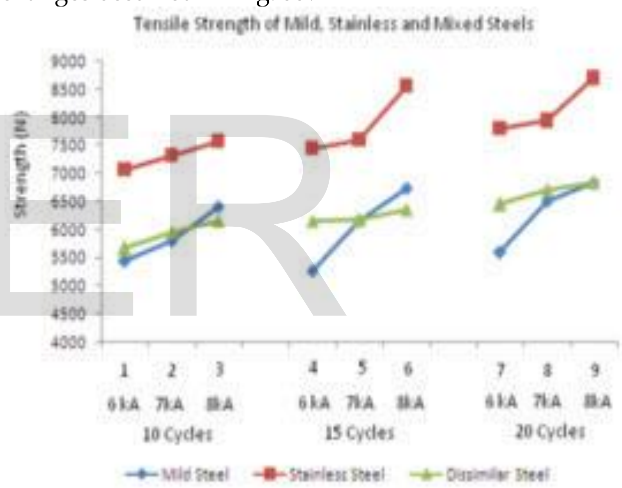

Fig. 35 — Tensile test results.

The stainlesssteel welds seemed to have higher tensilestrength compared to the other two typesof joints. In the mixedsteel joint, the mild steel side was brokenfirst. Button pull out, tear at the edge of one side and tear at the edge of both sides were common failure modes of the joints.

If a comparison study of strength between categoriesis considered, then the mild andstainless steels have created upper andlower strength bands and the dissimilarjoints almost fall between these two.

7.3 Analysis using Micrograph Views

A typical macrostructure for mild steel,stainless steel, and mixed steels showed three distinct structural zones viz.,Fusion Zone, Heat affected

Zone and base metal. For mild steel, the fusion zone consisted of coarser grains and the HAZ of finergrains with higher width compared to stainless steel due to better thermal conductivity and higher electrical resistivity. In contrast, the stainless steel had a lower width of HAZ and therefore the fusion zone seemed to be higher as compared to mild steel for the same weld schedule.

In case of mild steel and stainless steel weldments ,the mild steel side was shorter in length as compared to stainless steel with different HAZs.

Also A. AravinthanAnd C. Nachimaniobserved that the mild steel have the highest nugget growth compared to the other two types of joints with respect to weld current and welding cycle.

8.RESISTANCE SPOT WELDING OF TRIP STEEL WITH SECOND PULSE CURRENT

V. H. Baltazar Hernandez, Y. Okita, And Y. Zhou (Ref 5) used Second Pulse Current in Resistance Spot Welding to weld TRIP Steel to study its effects on the microstructure and mechanical behaviour of weldments.

Literature review suggested that due to higher alloying contents of TRIP steels,it had poorweldabilityshown by inconsistent interfacial failure(IF) or partial interfacial (PI) failuremodes coupled with diminished mechanicalperformance that are observed while welding TRIP steel using resistance spotwelding (Refs.27,28,29).

V. H. Baltazar Hernandez, Y. Okita, And Y. Zhoumade a systematic study on resistance spot welding of TRIP800(Tensile strength of 800MPa) steel sheets by applying local post-weld heat treatments through second impulse current in order to modify the fusion zone microstructure and, consequently, the mechanical performance. The chemical composition of TRIP800 is given in table 1.This steel is also known as Si-alloyed TRIP steel due to higher Si content.

The carbon equivalent of the TRIP steel as calculated byYurioka's (Ref. 30) was 0.527.TRIP steel shows transformation temperaturesMs, the critical transformation temperaturesAc1 and Ac3 as calculated usingequations reported earlier (Ref. 31) to be 3180C,7470C and 9150C respectively.

The base metal of TRIP steel showed ferrite matrix ,bainite , martensite, and retained austenite(volume fraction 12%) , as illustrated inFig. 36.

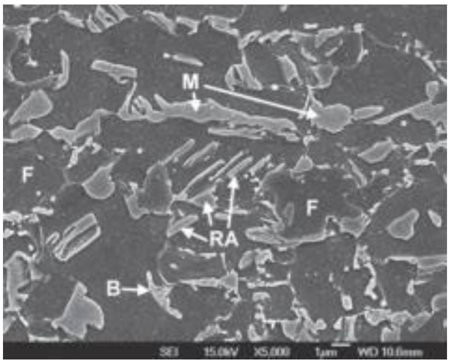

Fig.36— Base metal microstructure of TRIP steel showing the ferrite (F) matrix,the islands of martensite (M), retained austenite (RA), and bainite (B).

Resistance spot welds were conducted on machines specified earlier and two differentkinds of welding procedures with same schedule (Table 3) in resistance spot welding were followed.In the first type ofprocedure, a conventionalwelding schedulewas applied to heat, melt, and subsequentlycool down the specimen.It consisted of a single-pulse current(SPC), and the post-weld heat treatment condition was performed by a secondpulse current at one of three different current levels. The schematic illustration of the welding schedules of SPC and two- pulse current (TPC) is depicted in Fig. 37.

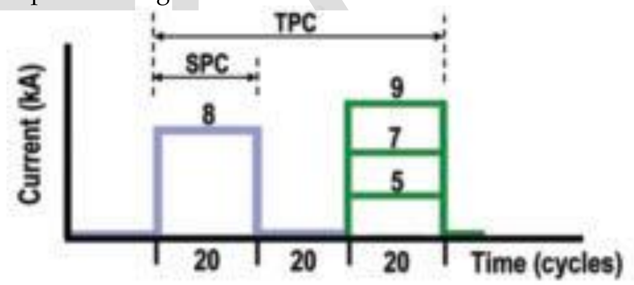

Fig. 37— Schematic of resistance spot welding pulsing current schedules. Single-pulse current (SPC) and two-pulse current (TPC).

Welding current kA	Second-pulse current kA	Force kN	Squeeze Time cycles	Hold time cycles	Cooling time between pulses cycles
8	5,7,9	4.5	25	5	20

Table 3 — Resistance Spot Welding Parameters

In second welding procedure aftermelting and cooling , a post-weldheat treatment was carried out in thespot welding machine by reheating thespecimen to a specific (aim) peak temperaturefollowed by rapid cooling.

A range ofcurrent levels between 5 and 9 kA with anincrement of 2 kA were applied in the secondpulse schedule/cycle. A cooling timeof 20 cycles was employed between the appliedpulses.

The weld nugget size was evaluated bymetallographic sample preparation techniques.Vickersmicro-hardness (HV) measurements wereperformed under a load of 200 g with adwell time of 15 s and maintaining a distanceof 200 μm between consecutiveindentations.

Quasi-static lap-shear tensile testswere conducted with an Instron 4206 universaltesting machine.

In order to understand thechanges in microstructure occurring dueto the application of varied second pulsecurrent procedures and to understand weld and post weld thermal history within nugget, numerical simulationsof single-pulse and two-pulse currentconditions were conducted. The weld thermalhistory within the fusion zone (FZ)was estimated through numerical simulation.The simulated thermal curves of all thefour conditions studied (i.e., SPC and TPCat 5, 7, and 9 kA) are shown in Fig. 38.

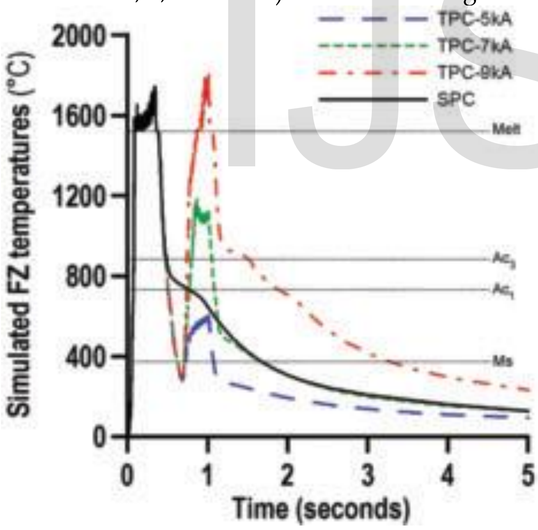

Fig. 38— Simulated welding thermal cycles for single-pulse (SPC) and two pulse current (TPC) conditions at different current levels.

It is clear from Fig 38that the first current impulseof the TPC specimens overlaps withthe SPC curve until the former reaches thecooling temperature of approximately800°C, and below this temperature theSPC and TPC curves separate.

8.1 Effect on Weld Nugget

Fig. 39 shows fusion zone, heat-affected zone (HAZ), and basemetal of the TRIP steel for SPC and TPC specimens. The FZ optical micrographs obtained from the weld nuggets for SPC welding condition and TPC welds are illustrated in Fig. 40.

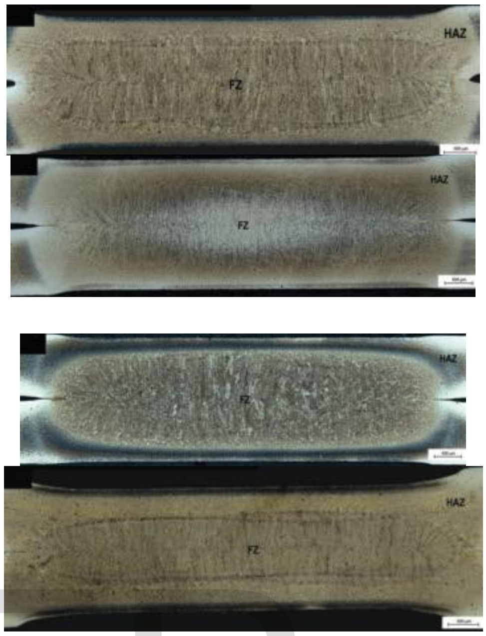

Fig. 39 — Cross-section macrostructures of TRIP steel resistance spot welded with the following: A —single-pulse current (8 kA), and second-pulse current of B — 5 kA; C — 7 kA; D — 9 kA.

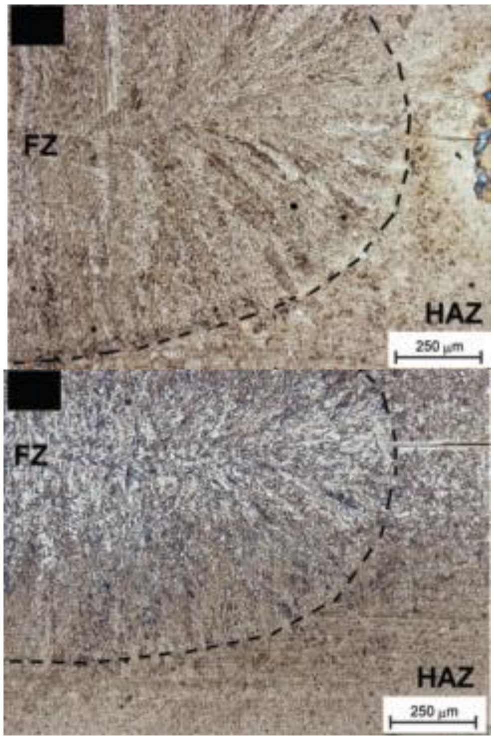

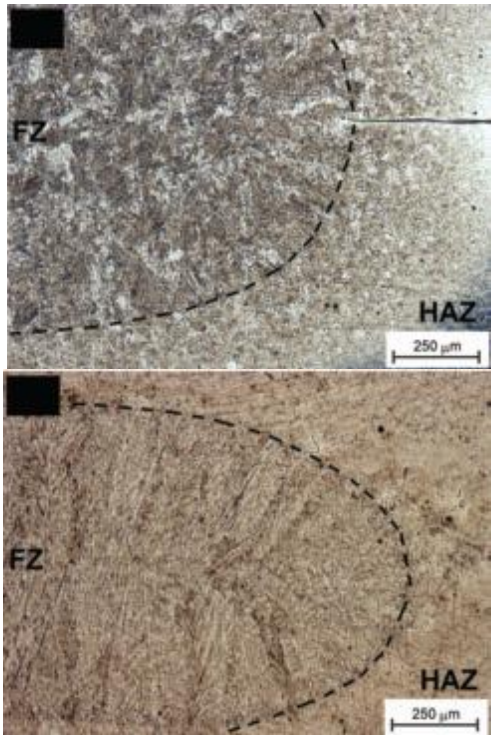

Fig. 40— Optical images illustrating the FZ microstructure in specimens subjected to the following: A —Single-pulse current (8 kA), and second-pulse current of B — 5 kA; C — 7 kA; D — 9 kA.

Dashed lines line in fig 40 shows weld interface. The macrostructure of the SPC specimen in Fig. 39 shows the periphery of the weld nugget clearly delineated whereas the FZ microstructure in Fig. 40 illustrateselongated columnar grain growth from the top and bottom weld interfaces towards centerline.The elongated columnar growth seemed influenced by the solidification path of the primary structure asstated in Ref 32that post-solidification weld microstructures are developed in the graininterior and/or along the grain boundaries of the primary structure .

The representative macrostructure of the TPC 5-kA specimens shown in Fig. 39 illustrates partially wiped out periphery of the weld nugget due to the effect of the post-weld heat treatment (TPC). Thus, the prior weld nugget appearance partially disappeared; instead, a brighter region evolved at the center of the nugget (Fig. 39) due to the effect of heat distribution during the second impulse current and formation of fine needle- and/or plate-like morphologies predominantly located at the centerline of the weld nugget as observed in Fig. 40.

Compared to the macrostructure of SPC specimen, TPC 7-kAspecimen (Fig. 39) shows that the originalperiphery of thenugget that formedduring the first pulse was barely visibleafter the second current impulse of TPC 7kA. The elongated columnar grain growth obtained during first impulse current seemed transformedinto an apparent quasi-equiaxedgrain morphology (during second impulsecurrent), which is confirmed in the FZ microstructure shown by Fig. 24C. This result confirmed that at intermediatevalues of secondimpulse current (i.e., 7 kA),the grain morphology developedduring the first impulsecurrent is transformedinto new grainsupon the second impulsecurrent, thus suggestinggrain recrystallization.

In the case of the TPC 9-kA specimen,a remelted nugget region with thinner appearance and new solidified macrostrucurewas observedoverlapped to the prior nugget of the firstcurrent impulse as depicted by Fig. 39. The formation of theremelted nugget with coarser elongated columnar grains (Fig 24D) can be attributed to thehigher current intensity of the second pulsecycle (9 kA).

The average weld nugget size measuredin the metallographic cross-sectionedsample is plotted in Fig. 41 for theSPC as well as the second pulse currentspecimens. It can be seen that the weldnugget size was constant at about 6 mm formost of the specimens, except the specimensubjected to the second current pulseof 9 kA (TPC 9 kA) that had a slightlylarger average nugget size.

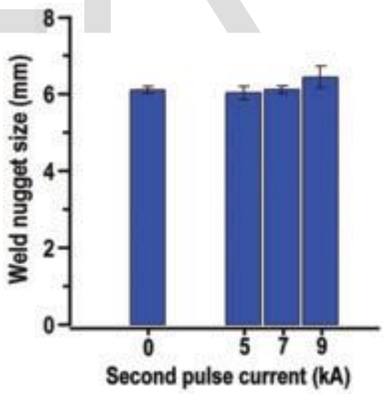

Fig. 41 — Weld nugget size by cross-sectioned measurements using metallographic techniques

8.2 EFFECT ON HARDNESS AND MICROSTRUCTURE

Figure 42shows the Vickers micro-hardnessprofiles of TRIP steel across the welded specimens from the centerof the nugget by ploting zero in thex axis and moving toward the base metal. The micro-hardnessof the base metal was found situatedat a distance of about 5 mm from the centerof the nuggetwith an average value of255 ± 4 HV. The maximum hardness valuesin the profiles (i.e., 520 and 545 HV forTPC 9 kA and SPC, respectively) werefound at the coarse grain region of theHAZ.

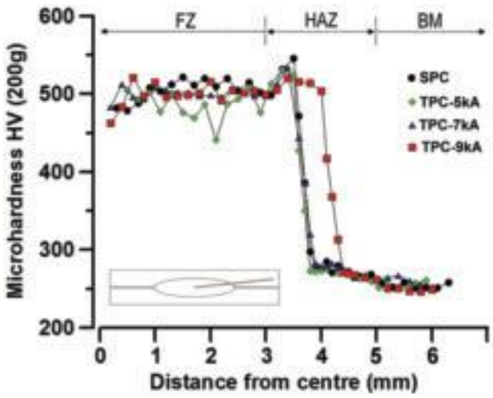

Fig. 42 — Vickers micro-hardness profiles across the weldment formed in different conditions studied. Micro-hardness was measured in the direction indicated in the inset image.

It should be noted thatremelting of the nugget had shifted the location of the maximum hardness for the TPC 9-kA specimen to theright as shown in Fig. 42. The average FZ hardness of theTPC 5-kA specimen (i.e., 476 HV) waslower with respect to that of the SPC specimen(i.e., 523 HV). The TPC 7 kA resultedin FZ hardness (i.e., 516 HV) comparableto that of the SPC specimen,whereas slightly lower FZ hardness (i.e.,505 HV) was measured for the TPC 9-kAspecimen.The microctructures of SPC , TPC 7 and 9 kA, predominantlyshowed martensite (M) laths with possible low volumefraction of upperbainite (B) located alongthe grain boundaries.In addition, microstructure of TPC 9-kA showed formation of side-plate structures of ferrite (F).On the other hand, the FZ microstructureof TPC 5-kA specimens revealed possibletempered martensite (TM) morphologyalong with considerable fraction of ferrite(F) in the form of elongated needleand/or plate-like morphology.Tempering ofmartensite in TPC 5-kA specimen seemedconsistent with a previous report on in-situtempering of TRIP steels (Ref. 33).

8.3 Analysis using joint tensile-shear performance

The average maximum lap-shear tensileload (failure) achieved in the specimensstudied is plotted in Fig. 43 as a functionof second pulse current.

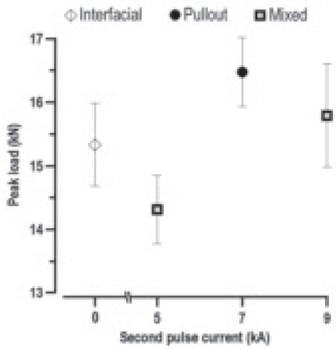

Fig. 43 — Maximum lap-shear tensile loads as a function of second-pulse current applied during RSW of TRIP steel.

It is to benoted that the peak load of the SPC specimencorresponds to zero second pulsecurrent of the graph and that of TPC specimenscorresponds to 5-, 7-, and 9-kA secondpulse current. Figure 44 illustratesrepresentative fractured surfaces obtainedafter the lap-shear tensile test of allthe specimens.

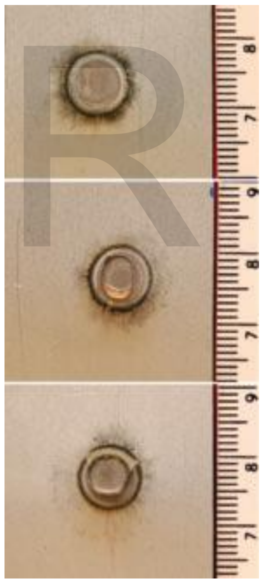

Fig. 44 — Representative lap-shear tensile failed specimens showing the following: A — Interfacial; B — partial interfacial; C — pullout failure modes.

An averaged maximum load of about15.3 ± 0.6 kN and interfacial failure mode (Fig 44) was obtained on the SPCspecimens. It was observed that the maximum failure load on TPC specimensvaried according to the second pulsecurrent level.Fifty percent of twopulsecurrent 5-kA specimens showed interfacial failure mode and remaining failed in partial interfacial mode as shown in Fig 44.All TPC 7-kA specimens showedcompletely pullout (PO) failureas depicted in Fig. 44.

The increase in the current level of the secondpulse (i.e., TPC- 9 kA) resulted in mixedfailures with 33% as Interfacial Failure, 17% as Partially Interfacial, and the remainingin Pull Out mode. The increased maximumload to failure for TPC 7 kA in comparisonto the other conditions is attributableto consistent pullout failures observed inthe full batch of assessed specimens. From Fig. 41it is clear that all the specimensshowed comparable weld nugget size with slightly larger nugget size inTPC-9kA specimen. Thus, it is conceivable to compareall the specimens with respect to theirload-bearing capacity. Hence, it is concludedthat the best lap-shear tensile performance,based on the peak load andfailure mode, was achieved in the TPC 7-kA condition — Figs. 43,44. It is to be noted that in spite of the slightly larger weldnugget size of the TPC 9-kA specimens, the load-bearing capacity did notimprove in comparison to that reached bythe TPC 7- kA specimens. Also it can be safely concluded that the second impulse current conditionstrongly influenced the failure mode ofTRIP steel, which in fact is associated withthe micro-structural changes occurring inthe weld nugget.

9 WELD PROPERTIES OF JOINTS

The results reported above are all of spot welds with different material but welded with lap joints with almost similar thickness. The weld properties and microstructure of the joints can be compared and can be related to different welding conditions.

9.1 Triple Thin Sheet Aluminum Alloy Resistance Spot Welds

The microstructure in the three-sheet 6061 aluminum alloy RSWs consisted of a partially melted zone (PMZ), columnar grain zone (CGZ), and equiaxed grain zone (EGZ), where the columnar grain zone is divided into the columnar grain with large secondary dendrite arm spacing (LCGZ) and the columnar grain with small secondary dendrite arm spacing (SCGZ). Three failure modes the interfacial (IF) failure, partial thickness-partial pull-out (PT-PP) failure, and pullout (PO) failure, were observed. The formation of the LCGZ in the weld nugget contributed to the PT-PP failure. Three failure modes in the Type IV joint, named the double interfacial (DIF) failure, one interfacial/one pullout (IF/PO) failure, and the base metal fracture (BMF) failure were identified.In the case of IF/PO failure, the weld nugget experienced less deformation due to its larger nugget size. In the case of BMF failure, the weld nugget had a very small deformation and the crack formed around the edge of the weld nugget and then propagated to the base metal. The cracks will form and propagate in the interior of the LCGZ or along the interface of SCGZ and LCGZ during the tensile-shear test as LCGZ is the weak area in three-sheet aluminum alloy RSWs. The equations were proposed to predict the critical nugget diameter required to ensure PO failure mode during the tensile-shear tests of three-sheet aluminum alloy spot weld joints.

9.2 Spot welding with magnetic assistance

Magnetically assisted resistance spot welding of 0.80-mm-thick DP980 steel was carried out and nugget formation was related to mode and intensity of an externally applied constant magnetic field .It was proved that growth rate of nugget diameter for the magnetically assisted weld with symmetric magnetic field was faster, nugget symmetry better with finer microstructures than that of the traditional weld was obtained, especially during the middle-late welding stage.Magnetically assisted welds were generally peanut-shell shaped with the nugget edges thicker than the middle showing further improvement with the increase in the external magnetic field intensity.Compared with the traditional welds under identical welding parameters, all the magnetically assisted welds exhibited higher tensile- shear strength, stronger energy absorption capacity, and higher probability of button-pullout fracture particularly under low welding current.

9.3 Dissimilar resistance spot welds in AISI 430 ferritic stainless steel and DQSK low-carbon steels

Fusion zone was featured by dual phase micro-structure of ferrite and martensite controlled by austenite stability. The amount of martensite depends on austenite formation at high temperature as well as the extremely high cooling rate of RSW.
The main metallurgical features in the HAZ of FSS side are grain growth and carbide precipitation whereas DQSK side was dictated by martensitic and eutectoid transformations. Increasing the welding current promoted double pullout mode. The DPF process could be divided into the following three stages: Stage I — work hardening and through thickness straining

of both sheets, Stage II — severe necking and occurring the first crack in the DQSK steel, and Stage III — formation of the second crack in the FSS side

9.4 Spot Welding of Mild steel and Stainless Steel

The investigation of spot weldnuggets' growth in mild steel, stainlesssteel, and dissimilar steels proved that the hardness of the welded zone isgreater than the hardness of the un-weldedzone for all three joints, increase in hardness being more in mild steel joint.Due to physical nature of stainless steel it gave higherweld strength compared to mild steel andthe mixed welds .The pull out breaksoccurred at the border of the weld (tearfrom edge) in majority of cases. Button pull outwas noticed for poor welds. Strength of the mixed weld (mildsteel and stainless steel) is almost similarto the strength of pure mild steel welds. The diameter of the nugget in stainlesssteel is bigger than the diameter ofnugget in mild steel for the same currentand weld time. Mild steel seemed to have the highestnugget growth rate as compared to theother two types of joints.

9.5 Resistance spot welding of TRIP Steel using second pulse current

Local post-weld heattreatments by second pulse currents in resistance spot welding was used to improve the fusion zone (FZ) microstructure and the mechanical behaviour of resistance spot welded TRIP steel. Upon conditions of intermediate levels ofsecond pulse current (i.e., 7 kA), improved lap-shear tensile behaviour such as pullout failure mode and increased maximum load to failure were achieved. Tempering of martensite along witha fraction of elongated plate-like ferritewas observed at the lower levels of secondpulse current (5 kA) coupled with a clearreduction in FZ hardness. However, noimprovement was observed in the lap-sheartensile behaviour. At the higher levels of second pulsecurrent (9 kA), re-melting and formationof a new solidified elongated columnarstructure of predominantly martensite microstructurewas seen in the fusion zone.The slight improvement in themechanical performance was due to theincreased size of the weld nugget duringre-melting.

References

1. 1.Y. Li, Y. Zhang, Z. Luo, H. Shan, Y. Q. Feng, And Z. X. Ling. 2016. Failure Mode Transition Of Triple Thin SheetAluminum Alloy Resistance Spot Welds UnderTensile ShearLoads. Welding Journal 95(12): 479-S To 490-S.
2. 2.Y. B. Li, Y. T. Li, Q. Shen, And Z. Q. Lin 2013 Magnetically Assisted Resistance Spot Welding of Dual-Phase Steel Welding Journal 92(4): 124-s to 132-s
3.
4. 3. M. Pouranvari, S. P. H. Marashi, And M. Alizadeh-Sh2015. Welding Metallurgy Of Dissimilar Aisi 430/Dqsk Steels Resistance Spot Welds. Welding Journal94(06): 203-S To 210-S.
5.
6. 4. A. Aravinthan And C. Nachimani2011Analysis of Spot Weld Growth on Mild and Stainless SteelWelding Journal 90(8): 143-s to 147-s
7.
8. 5. V. H. Baltazar Hernandez, Y. Okita, And Y. Zhou 2012 Second Pulse Current in Resistance Spot Welded TRIP Steel — Effects on the Microstructure and Mechanical BehaviorWelding Journal 91(10): 278-s to 285-s
9.
10. 6. Hongyan, Z., And Jacek, S. 2012. Resistance Welding: Fundamental And Applications, 2nd Ed. Boca Raton, Crc Press.
11. 7. Drebushchak, V. A. 2008. The Peltier Effect. Journal Of Thermal Analysis AndCalorimetry91(1): 311–315.
12. 8. Li, B. Q. 2002. Research on the numerical Simulation of the Process for Aluminum AlloyResistance Spot Welding and Energy Analysis. PhD Dissertation. Tianjin, Tianjin University .
13. 9. Pouranvari, M., Marashi, S. P. H., and Mousavizadeh, S. M. 2010. Failure mode transition and mechanical properties of similar and dissimilar resistance spot welds of DP600 and low carbon steels. Scienceand Technology of Welding and Joining 15(7): 625–631
14. 10. Han, L., Thornton, M., Boomer, D., and Shergold, M. 2011. A correlation study of mechanical strength of resistance spot welding of AA5754 aluminium alloy. Journalof Materials Processing Technology 211: 513–521.
15. 11. Sun, X., Stephens, E. V., Davies, R. W., Khaleel, M. A., and Spinella, D. J. 2004. Effects of fusion zone size on failure modes and static strength of aluminum resistance spot welds. Welding Journal 83(11): 308-s to 318-s.
16.
17. 12. Pouranvari, M., Asgari, H. R., Mosavizadch, S. M., Marashi, P. H., and Goodarzi, M. 2007. Effect of weld nugget size on overload failure mode of resistance spot welds. Science and Technology of Weldingand Joining 12(3): 217–225.
18. 13. Pouranvari, M., and Marashi, S. P. H. 2012. Failure mode transition in AISI 304 resistance spot welds. Welding Journal 91(11): 303-s to 309-s.
19. 14. VandenBossche, D. J. 1977. Ultimate strength and

failure mode of spot welds in high strength steels. SAE TechnicalPaper 770214: 955–966.

20. 15. Pouranvari, M., and Marashi, S. P. H. 2013. Critical review of automotive steels spot welding: Process, structure and properties. Science and Technology of Weldingand Joining 18(5): 361–403
21. 16. Pouranvari, M., Asgari, H. R., Mosavizadch,S. M., et al. 2007. Effect of weld nugget size on overload failure mode of resistance spot welds. Science and Technology of Welding andJoining 12(3): 217-s to 225-s.
22. 17. Recommended practices for test methods for evaluating the resistance spot welding behavior of automotive sheet steel materials. ANSI/AWS/SAE/D89-97. Miami, Fla.: AWS; 1997.
23. 18. Alizadeh-Sh, M., Marashi, S. P. H., and Pouranvari, M. 2014. Resistance spot welding of AISI 430 ferritic stainless steel: Phase transformations and mechanical properties. Materials and Design 56: 258–63.
24. 19. Pouranvari, M., and Marashi, S. P. H. 2013. Critical review of automotive steels spot welding: process, structure and properties. Science Technology Welding Joining 18: 361–403.
25. 20. Self, J. A., Olson, D. L., and Edwards, G. R. 1987. The stability of austenitic weld metal. NBS Publication onCryogenic Properties of Metals: 181–189
26. 21. Lippold, J. C., and Kotecki, D. J. 2005. Welding Metallurgy and Weldability ofStainless Steels. New Jersey: John Wiley & Sons.
27. 22. Lippold, J. C., and Kotecki, D. J. 2005. Welding Metallurgy and Weldability ofStainless Steels. New Jersey: John Wiley & Sons.
28. 23.Pouranvari, M., and Marashi, S. P. H. 2011. Failure mode transition in AHSS resistance spot welds. Part I. Controlling factors. Materials Science Engineering A 528: 8337–43.
29. 24. Kong, X., Yang, Q., Li, B., Rothwell, G., English, R., and Ren, X. J. 2008. Numerical study of strengths of spot-welded joints of steel. Materials and Design 29: 1554–1561
30. 25. Sun, D. Q., Lang, B., Sun, D. X., and Li, J. B. 2007. Microstructures and mechanical properties of resistance spot welded magnesium alloy joints. Materials Science and Engineering App. 460–461, 494–498.
31.
32. 26. von Maubeuge, K. P., and Naue, H. E. 2000. Comparison of peel bond and shear tensile test methods for needle punched geosynthetic clay liners. Geotextiles and Geomembranes18: 203–214.
33.
34. 27. Smith, S., and den Uijl, N. 2006. Resistance spot welding of advanced high strength steels for the automotive industry. The 4th InternationalSeminar on Advances in ResistanceWelding. Wels, Austria, pp. 30–60.
35.
36. 28. Khan, M. I., Kuntz, M. L., Biro, E., and Zhou, Y. 2008. Microstructure and mechanical properties of resistance spot welded AHSS. Mater. Trans., JIM, 49(7): 1629–1637.
37.
38. 29. Rathbun, R. W., Matlock, D. K., and Speer, J. G. 2003. Fatigue behaviour of spot welded high-strength sheet steels. Welding Journal 82(8): 207-s to 218-s.
39.
40. 30. Yurioka, N., Suzuki, H., Ohshita, S., and Saito, S. 1983. Determination of necessary preheating preheating temperature in steel welding. WeldingJournal 62(6): 147–153.
41.
42. 31. Yurioka, N. Weldability calculation, http://homepage3.nifty.com/yurioka/ exp.html. Accessed on Nov. 11, 2009.
43.
44. 32. Kou, S. 2003. Welding Metallurgy. Wiley-Interscience, 2nd ed., p. 232
45.
46. 33. Chuko, W. L., and Gould, J. E. 2002. Development of appropriate resistance spot welding practice for transformation-hardenedsteels. Welding Journal 81(1): 1-s to 7-s.